

# Hollow Anatase TiO<sub>2</sub> Single Crystals and Mesocrystals with Dominant {101} Facets for Improved Photocatalysis Activity and Tuned Reaction Preference

Wei Jiao,<sup>†</sup> Lianzhou Wang,<sup>‡</sup> Gang Liu,<sup>\*,†</sup> Gao Qing (Max) Lu,<sup>‡</sup> and Hui-Ming Cheng<sup>†</sup>

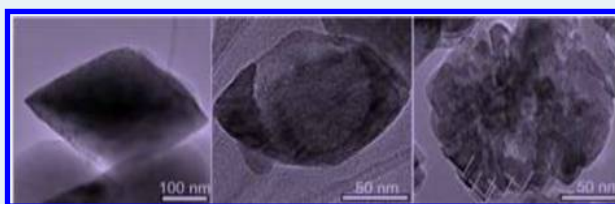
<sup>†</sup>Shenyang National Laboratory for Materials Science, Institute of Metal Research, Chinese Academy of Sciences, 72 Wenhua RD, Shenyang 110016, China

<sup>‡</sup>ARC Centre of Excellence for Functional Nanomaterials, The University of Queensland, Qld. 4072, Australia

## S Supporting Information

**ABSTRACT:** Faceting photocatalysts has attracted increasing interest to improve photocatalytic activity by optimizing surface charge carrier separation/transfer. In principle, a high photocatalytic activity is co-contributed by both high surface separation/transfer and low bulk recombination of charge carriers. However, little effort focuses on lowering bulk recombination of charge carriers in faceted photocatalysts. In this work, we report the synthesis of hollow anatase TiO<sub>2</sub> single crystals and mesocrystals with dominant {101} facets by a new route with PO<sub>4</sub><sup>3-</sup>/F<sup>-</sup> as morphology controlling agent. It is found that with respect to solid crystals, being hollow crystals and mesocrystals can substantially improve photocatalytic activity (O<sub>2</sub>/H<sub>2</sub> evolution from water splitting, CH<sub>4</sub> generation from photoreduction of CO<sub>2</sub>) as a result of the synergistic effects of shortened bulk diffusion length of carriers for the decreased bulk recombination and increased surface area. Furthermore, the photocatalysis reaction preference toward O<sub>2</sub> and H<sub>2</sub> evolution from water splitting can be tuned.

**KEYWORDS:** hollow TiO<sub>2</sub>, single crystal, mesocrystal, photocatalysis



## INTRODUCTION

Developing semiconductor photocatalysts with certain well-defined facets is becoming an important strategy to improve their photocatalytic activity and/or tune their reaction preferences toward different applications.<sup>1,2</sup> The base of this strategy is that both the activity and the preference of photocatalytic reactions are sensitive to the surface atomic structure and electronic structure, which varies with different crystallographic orientations, of the photocatalyst crystals. Maximizing the surface of a photocatalyst to reactive facets is feasible to realize such a goal. Anatase TiO<sub>2</sub> crystals as one of the most important photocatalysts have been increasingly investigated in terms of well-defined facets since Yang et al. obtained a large percentage of high-energy {001} (ca. 47%) in micrometer-sized crystals.<sup>3</sup> So far, various modified synthesis routes have been developed to prepare the crystals with a higher percentage of {001} and smaller particle size so that the photocatalytic activity may be further improved.<sup>4–10</sup> On the other hand, it has been revealed that low index facets of anatase TiO<sub>2</sub> follows a reactivity order of {001} < {101} < {010} by statistically comparing photocatalytic hydrogen evolution and •OH radical generation from the crystals with a predominance of {001}, {101}, and {010}.<sup>11</sup> Tachikawa et al. also showed a consistent conclusion of {101} being more reactive than {001} by monitoring the reactivity of a single particle.<sup>12</sup> Achieving crystals with dominant {101}/{010}, therefore, deserves more attention.<sup>13,14</sup>

Equally important to acquiring the above reactive facets for promoting surface charge carrier separation/transfer, decreasing serious bulk carrier recombination will definitely contribute to the photocatalytic activity. The most widely used strategy is to shorten the bulk diffusion length of carriers by decreasing particle size particularly to nanoscale. Notwithstanding its effectiveness, the apparent drawback of this strategy includes serious agglomeration of nanosized particles causing not only a decreased surface area but also increased grain boundary recombination. Being hollow in single crystal or even mesocrystal enclosed with reactive facets might be an alternative to overcome this drawback.<sup>15,16</sup> In this work, we developed a facile route using F<sup>-</sup>/PO<sub>4</sub><sup>3-</sup> as a morphology-controlling co-mediator to one-pot synthesize hollow anatase TiO<sub>2</sub> single crystals and mesocrystals with dominant reactive {101} facets. Compared with a control sample, solid crystals with {101}, the hollow crystals show not only superior photocatalytic activities but also the ability of tuning reaction preferences in photocatalytic hydrogen and oxygen evolutions from water splitting, and photoreduction of CO<sub>2</sub> to CH<sub>4</sub>.

Received: April 8, 2012

Revised: June 30, 2012

Published: July 31, 2012

## EXPERIMENTAL METHODS

**Sample Synthesis.** Hydrofluoric acid (HF) (50 wt %, *Caution! very corrosive.*) was used to obtain HF solution with different concentrations (300 mM, 400 mM, 500 mM). In a typical synthesis route, 1.2 g of titanium sulfate ( $\text{Ti}(\text{SO}_4)_2$ ) and 0.9 g of sodium phosphate ( $\text{Na}_3\text{PO}_4$ ) powder were one by one dissolved in 40 mL of HF solution. The obtained aqueous solution was then transferred to a Teflon-lined autoclave, and treated at 180 °C for 12 h. After reaction, the products were collected by centrifugation method and washed with deionized water 3 times to remove dissoluble ionic impurities. Then the samples were dried at 90 °C in air. In the control experiments, all reaction conditions were kept unchanged except that no  $\text{Na}_3\text{PO}_4$  (HF) was introduced in the reaction solution. To further show the synergistic effect of HF and  $\text{Na}_3\text{PO}_4$ , the synthesis of  $\text{TiO}_2$  crystals in HCl solution containing  $\text{Na}_3\text{PO}_4$  was conducted.

**Characterization.** X-ray diffraction (XRD) patterns of the samples were recorded on a Rigaku diffractometer using Cu irradiation. Their morphology and crystalline structure were determined by scanning electron microscopy (SEM) and transmission electron microscopy (TEM) performed on a SUPRA 35 and JEOL 2010. The Brunauer–Emmett–Teller (BET) surface area was determined by nitrogen adsorption–desorption isotherm measurements at 77 K (ASAP 2010). Raman spectra were collected with LabRam HR 800. Chemical compositions and valence band spectra of the  $\text{TiO}_2$  samples were analyzed using X-ray photoelectron spectroscopy (Thermo Escalab 250, a monochromatic Al  $K_{\alpha}$  X-ray source). All binding energies were referenced to the C 1s peak (284.6 eV) arising from adventitious carbon. The optical absorbance spectra of the samples were recorded in a UV–visible spectrophotometer (JASCO V-550).

**Photocatalytic Activity Measurements.** Photocatalytic hydrogen and oxygen evolution reactions were carried out in a top-irradiation vessel connected to a glass-enclosed gas circulation system. 100 mg of the  $\text{TiO}_2$  powder was dispersed in 300 mL aqueous solution containing 10 vol% methanol for hydrogen evolution or 16.7 mM  $\text{AgNO}_3$  for oxygen evolution. The reaction temperature was maintained around 20 °C. The amount of  $\text{H}_2$  and  $\text{O}_2$  evolved was determined using a gas chromatograph (Agilent Technologies: 6890N).

The photoreduction experiments of  $\text{CO}_2$  were conducted in a homemade Teflon-lined stainless reaction chamber with a quartz window at the top for light irradiation. The volume of the chamber was 50  $\text{cm}^3$ . A 50 mg portion of the  $\text{RuO}_2$ -loaded sample was laid at the bottom of the reaction chamber. Prior to filling the gaseous  $\text{CO}_2$ , the chamber was evacuated by a mechanical pump. Then,  $\text{CO}_2$  bubbled from water was added to the chamber to reach a pressure of 0.06 MPa. The total amount of products generated in the chamber after light irradiation was determined by analyzing a 1.0 mL gas from the chamber with a gas chromatograph (Agilent Technologies: 6890N). The light source was a 300 W Xe lamp (Beijing Trusttech Co. Ltd., PLS-SXE-300UV).

## RESULTS AND DISCUSSION

In a typical synthesis, 1.2 g of titanium sulfate ( $\text{Ti}(\text{SO}_4)_2$ ) and 0.9 g of sodium phosphate ( $\text{Na}_3\text{PO}_4$ ) dissolved in 40 mL of hydrofluoric acid (HF) solution was hydrothermally treated at 180 °C in a Teflon-lined stainless steel autoclave. After reaction for 12 h, the products of solid and hollow crystals were

obtained sensitively depending on the HF concentration used. SEM images in Figures 1A–C show the uniform and well-

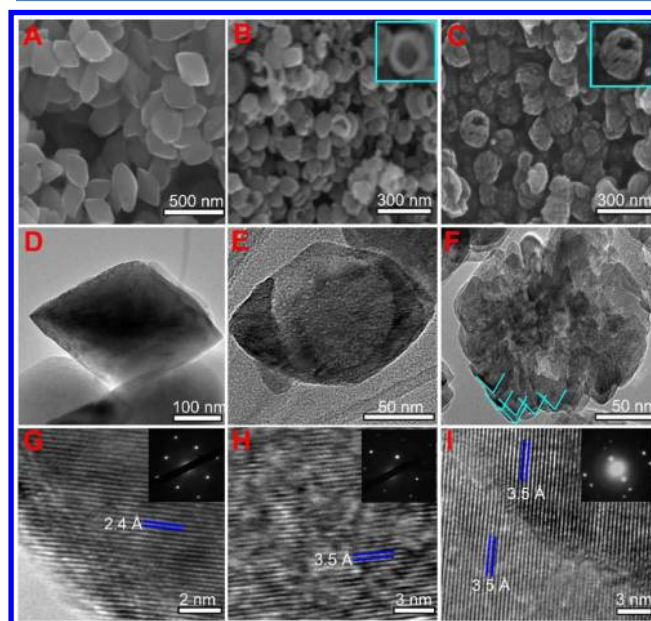


**Figure 1.** SEM, TEM, and HRTEM images of (A, D, G) solid anatase  $\text{TiO}_2$  single crystals, (B, E, H) hollow anatase  $\text{TiO}_2$  single crystals, and (C, F, I) hollow anatase  $\text{TiO}_2$  mesocrystals with  $\{101\}$  facets. The insets in (B) and (C) are the SEM images of representative hollow single crystal and mesocrystal particles. The insets in (G), (H), and (I) are the corresponding selected area electron diffraction (SAED) patterns recorded from a whole solid single crystal, hollow single crystal, and mesocrystal particle.

dispersed crystals synthesized. With 500 mM HF, solid crystals in an octahedral shape have a top-to-top length of about 400 nm (Figure 1A), which is further confirmed by a TEM image of a single particle (Figure 1D). On the basis of the crystallographic symmetries and Wulff construction of anatase  $\text{TiO}_2$  under equilibrium conditions,<sup>17</sup> it is easy to identify the 8 equivalent facets of the octahedron as the thermally most stable  $\{101\}$ . By lowering the HF concentration to 400 mM, the crystal size decreases to about 160 nm. Furthermore, a hollow inner structure is formed in the crystal with a basically retained octahedron morphology (See Figures 1B and E). It is worth noting that, similar to the solid octahedron crystal, the hollow octahedron crystal retains well a single crystalline nature as indicated by one set of SAED pattern and clear lattice fringes with one crystallographic orientation in Figures 1G and H. In addition, the shape of hollow octahedron crystals is not as sharp as that of solid octahedron crystals probably because of some coexistence of minor high-index facets such as  $\{103\}$  besides major  $\{101\}$ .<sup>18</sup>

Further lowering the HF concentration to 300 mM leads to the formation of sphere-like hollow cages with a diameter of about 150 nm (Figure 1C). TEM image in Figure 1F reveals that the cage wall consists of tiny octahedron crystals with a length of about 35 nm as indicated by dot lines. It is interesting to note that the arrangement of nearly all these tiny octahedra shares the same crystallographic orientation of  $[001]$  as a result of spontaneous self-organization of adjacent tiny octahedra to reduce the total surface energy during crystal growth. The nature of the hollow cage as mesocrystal can be clearly suggested by SAED patterns and high resolution TEM

(HRTEM) in Figure 1I. Different from the typical SAED diffraction rings of common nanocrystal agglomerates, the hollow cages give a single-crystal-like regular SAED pattern though a few weak irregular spots occasionally appear in the inset of Figure 1I. HRTEM image of the boundary area of two adjacent tiny octahedra shows a sole set of lattice fringes with a space of 3.5 Å, which is assigned to the {101} facet, suggesting the merger of adjacent tiny octahedra, to some extent. The merging can also be supported by the slight broadening of X-ray diffraction peaks of hollow mesocrystals consisting of tiny nano-octahedra with respect to that of solid and hollow single crystal octahedra (Supporting Information, Figure S1).

X-ray photoelectron spectroscopy (XPS) was used to determine the surface chemical compositions and chemical states of the resultant crystals. Both phosphorus and fluorine were present in the crystals with the apparent XPS signals of P 2p and F 1s in Figure 2. The phosphorus with a binding energy

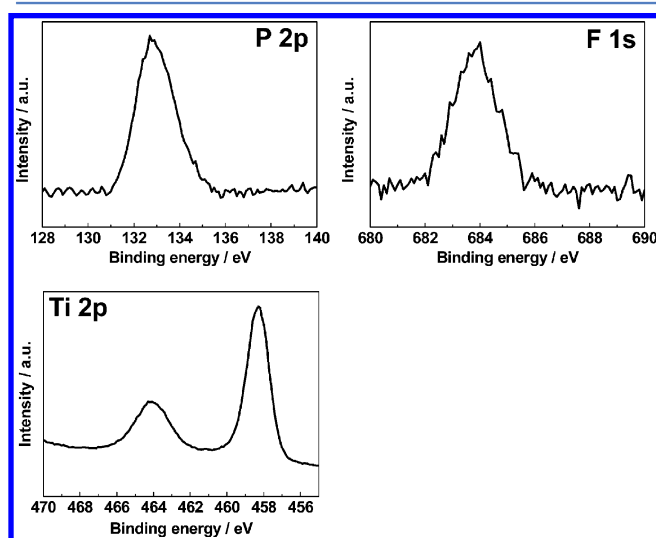


**Figure 2.** Typical high resolution XPS spectra of P 2p, F 1s, and Ti 2p in the synthesized anatase TiO<sub>2</sub> crystals with dominant {101} facets.

of 132.8 eV originates from P–O bonds in surface terminated PO<sub>4</sub><sup>3−</sup> groups. The detected fluorine species with a binding energy of 683.8 eV is identified as surface Ti–F bonds.<sup>3,19</sup> The smaller binding energy of F 1s by 0.3 eV than that in phosphorus-free TiO<sub>2</sub><sup>20</sup> could be caused by the interaction between surface PO<sub>4</sub><sup>3−</sup> groups and F<sup>−</sup>. The chemical state of Ti (Ti 2p<sub>3/2</sub>, binding energy: 458.3 eV) is identical to that of previously reported anatase TiO<sub>2</sub>.<sup>20</sup> The atomic percentage of fluorine (phosphorus) in the solid and hollow single crystals, and hollow mesocrystals is 1.1% (2.7%), 1.1% (1.0%), 1.3% (2.3%), respectively.

It is necessary to discuss why the presence of a high percentage of surface Ti–F bonds in this case does not result in a predominance of {001} facets as usual. The effectiveness of Ti–F bonds in reversing the relative stability of the highest energy {001} and lowest energy {101} has been solidly established in the literature.<sup>3–9</sup> Furthermore, the synergistic effects of additional capping agents such as the alkoxy group ((CH<sub>3</sub>)<sub>2</sub>CHO<sup>−</sup>) with F<sup>−</sup> were also found to increase the percentage of {001} by strengthening surface Ti–F bonds.<sup>5</sup> Here, it is reasonable to consider that the PO<sub>4</sub><sup>3−</sup> groups play a substantial role in counteracting the effects of Ti–F bonds on stabilizing {001} through the interaction between surface

PO<sub>4</sub><sup>3−</sup> groups and F<sup>−</sup>, which is partially indicated by the shifted binding energy of fluorine. Specifically, because of the large ionic diameter of PO<sub>4</sub><sup>3−</sup> groups, the obvious steric hindrance as a result of the adsorbed PO<sub>4</sub><sup>3−</sup> groups on TiO<sub>2</sub> surface will weaken the Ti–F bonds. Although the Ti–F bonds formed would not contribute to the formation of {001}, they still exert obvious influence on modifying the force constants of Ti–O–Ti framework as indicated by Raman spectra of the crystals (Supporting Information, Figure S2). Specifically, the relative intensity order of active modes B<sub>1g</sub> at 393 cm<sup>−1</sup> and A<sub>1g</sub> at 514 cm<sup>−1</sup> is reversed with respect to that of clean anatase TiO<sub>2</sub>. Similar results were also evidenced in fluorine terminated TiO<sub>2</sub> crystals.<sup>1,20</sup>

To determine the key factors controlling the formation of the hollow single crystals and mesocrystals, we conducted control synthesis experiments by changing different additives in the hydrothermal synthesis. As shown in Figure 3, sole F<sup>−</sup> only

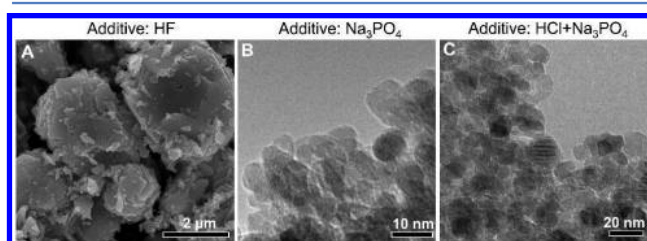


**Figure 3.** SEM (A) and TEM (B, C) images of anatase TiO<sub>2</sub> samples synthesized with different additives in the aqueous solution: A, only HF; B, only Na<sub>3</sub>PO<sub>4</sub>; C, HCl and Na<sub>3</sub>PO<sub>4</sub>.

results in micrometer-sized crystals with usually observed {001}. In contrast, sole PO<sub>4</sub><sup>3−</sup> leads to the formation of TiO<sub>2</sub> nanoparticles with the particle size of less than 10 nm. The coupling of Cl<sup>−</sup> and PO<sub>4</sub><sup>3−</sup> also results in similar TiO<sub>2</sub> nanoparticles. On the basis of these results, it is determined that the coexistence of F<sup>−</sup> with PO<sub>4</sub><sup>3−</sup> is crucial for growing the hollow crystals with dominant {101} facets. Several mechanisms such as the Ostwald ripening, gas bubbling, and etching can result in a hollow structure. In the case of hollow single crystals, a subsequent etching process after the full crystal growth may contribute to the hollow core formation as observed in hollow {001} dominant TiO<sub>2</sub>,<sup>21</sup> and the Ostwald ripening process after the tiny crystal agglomeration is responsible for the formation of hollow mesocrystals as observed in hollow CeO<sub>2</sub> mesocrystals.<sup>22</sup>

We have investigated the photocatalytic behaviors of the resultant crystals by monitoring photocatalytic hydrogen and oxygen evolution from water splitting in the presence of electron and hole donors, and photocatalytic conversion of CO<sub>2</sub> to CH<sub>4</sub> in the presence of water vapor. As shown in Figure 4, the hollow single crystals and mesocrystals show much superior activities to the solid single crystals in all three reactions investigated. The specific surface areas of solid single crystals, hollow single crystals, and hollow mesocrystals are 17, 35, and 42 m<sup>2</sup> g<sup>−1</sup> (Supporting Information, Figure S3). The increased surface area due to the hollow structure and decreased particle size is definitely useful for improving the activities by providing abundant potential reactive sites. The underlying factor accounting for the improvement is a greatly shortened bulk diffusion length of charge carriers for decreasing bulk recombination associated with the hollow structures, particularly when one considers a factor of 4–5 improvement in H<sub>2</sub> evolution and CH<sub>4</sub> generation in Figures 4 A and C. In



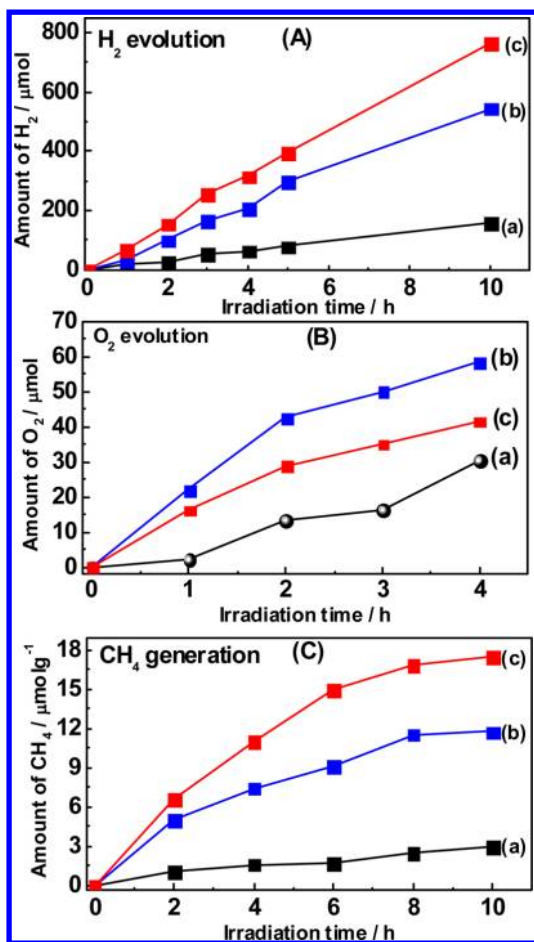


**Figure 4.** (A) Photocatalytic hydrogen evolution from 2 wt % Pt loaded photocatalysts in the presence of methanol as an electron donor; (B) photocatalytic oxygen evolution from bare photocatalysts in the presence of  $\text{AgNO}_3$  as a hole donor; (C) Photocatalytic reduction of  $\text{CO}_2$  to  $\text{CH}_4$  in the presence of water vapor from 1 wt %  $\text{RuO}_2$  loaded photocatalysts: (a) solid and (b) hollow anatase  $\text{TiO}_2$  single crystals, and (c) hollow anatase  $\text{TiO}_2$  mesocrystals, with dominant {101}.

addition, the hollow structure is also beneficial for the photodegradation of Rhodamine B (Supporting Information, Figure S4).

It is considered that heterogeneous catalysis can be sensitively affected by the distribution of metals on substrates. To determine whether the activity difference observed in our case is caused by photocatalysts themselves instead of different cocatalyst dispersion, we first compared the dispersion of Pt nanoparticles on three kinds of  $\text{TiO}_2$  crystals. As shown in Figure 5, the dispersion of Pt nanoparticles with the size of several nanometers on three different  $\text{TiO}_2$  crystals is basically comparable, suggesting that the dispersion of cocatalyst should not be the key reason for the activity difference. This claim can be convincingly supported by directly comparing the photocatalytic hydrogen evolution from three kinds of bare  $\text{TiO}_2$  crystals. Their reaction order is consistent with that of the Pt loaded photocatalysts (Figure 6), though the absolute activity of  $\text{TiO}_2$  crystals without Pt loading is very low. It is therefore clear that the activity difference of Pt loaded  $\text{TiO}_2$  originates from the different properties of  $\text{TiO}_2$  crystals instead of Pt loading.

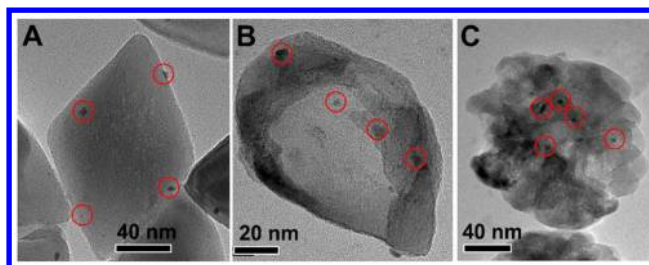


**Figure 5.** TEM images of 1 wt % Pt loaded photocatalysts: solid (A) and hollow (B) anatase  $\text{TiO}_2$  single crystals, and hollow anatase  $\text{TiO}_2$  mesocrystals (C), with dominant {101}.

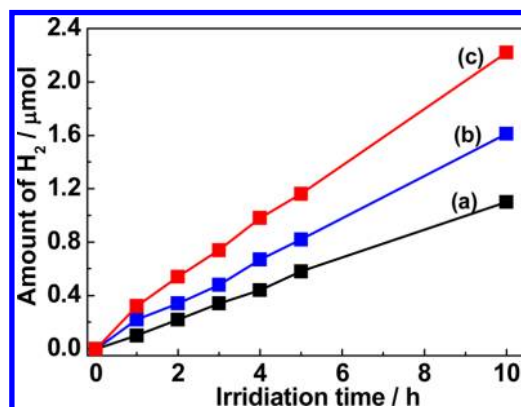


**Figure 6.** Photocatalytic hydrogen evolution from bare photocatalysts without loading of cocatalyst in the presence of methanol as an electron donor: (a) solid and (b) hollow anatase  $\text{TiO}_2$  single crystals, and (c) hollow anatase  $\text{TiO}_2$  mesocrystals, with dominant {101}.

Although the hollow single crystals have a comparable surface area to the hollow mesocrystals, they exhibit different reaction preferences. The hollow mesocrystals are more active in  $\text{H}_2$  evolution and  $\text{CH}_4$  generation, but less active in oxygen evolution than the hollow single crystals. The photocatalytic reaction preference is inherently controlled by the electronic band structure of photocatalysts. UV–visible absorption spectra in Figure 7A show that the solid single crystals and hollow

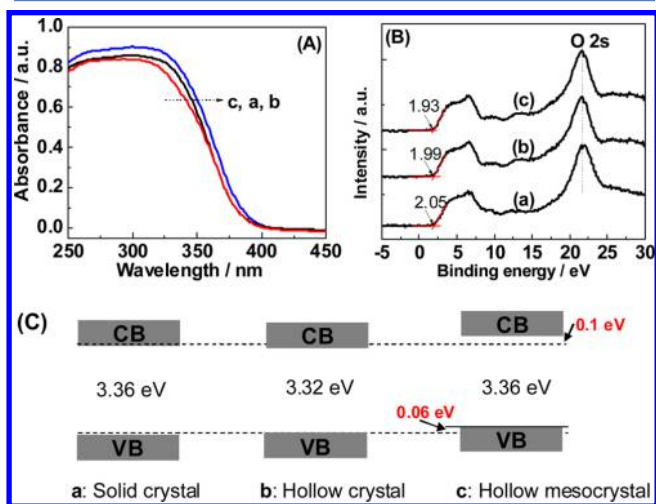


**Figure 7.** (A) UV–visible absorption spectra, (B) XPS valence band spectra, and (C) schematic electronic band structures of (a) solid anatase  $\text{TiO}_2$  single crystals, (b) hollow anatase  $\text{TiO}_2$  single crystals, and (c) hollow anatase  $\text{TiO}_2$  mesocrystals with dominant {101} facets.

mesocrystals have a marginally larger bandgap than the hollow single crystals. XPS valence band spectra in Figure 7B give different valence band maxima of three kinds of TiO<sub>2</sub> crystals. The difference in the bandgap and valence band maximum can be caused by two factors. One is the lower amount of PO<sub>4</sub><sup>3-</sup> on the hollow single crystals than on the other two (1.0% vs 2.7%/2.3%). It is reported that surface terminated phosphate groups on TiO<sub>2</sub> can increase the bandgap;<sup>23</sup> the other is the different abundance of {101} in each sample. Previous work has clearly demonstrated that both the bandgap and the band edges of photocatalysts can be tuned as a result of the exposure of different facets.<sup>11,20,24</sup> In our case, the solid crystals with sharp edges and smooth facets are well developed, and their surface consists of {101} facets. In contrast, the hollow single crystals and mesocrystals are not fully developed, and their surface consists of major {101} and also minor high-index facets.

On the basis of a combined analysis of UV–visible absorption spectra and valence band spectra, the hollow mesocrystals are determined to have higher conduction and valence band edges than the hollow single crystals (Figure 7C). That is, the photoexcited electrons from the hollow mesocrystals are more active in reducing H<sub>2</sub>O for H<sub>2</sub>, which is the rate-limiting step in the presence of an electron donor; while the photoexcited holes from the hollow single crystals are more active in oxidizing H<sub>2</sub>O for O<sub>2</sub>, which is the rate-limiting step in the presence of an electron acceptor. In the case of CH<sub>4</sub> generation, both the reduction of CO<sub>2</sub> and the oxidation of H<sub>2</sub>O represent multicarrier transfer processes ( $2\text{H}_2\text{O} + 4\text{h}^+ \rightarrow \text{O}_2 + 4\text{H}^+ + 4\text{e}^-$ ,  $E^0(\text{O}_2/\text{H}_2\text{O}) = 0.82 \text{ V}$ ;  $\text{CO}_2 + 8\text{e}^- + 8\text{H}^+ \rightarrow \text{CH}_4 + 2\text{H}_2\text{O}$ ,  $E^0(\text{CO}_2/\text{CH}_4) = -0.24 \text{ V}$  vs NHE), making the overall reaction efficiency low. That the hollow mesocrystals show a higher CH<sub>4</sub> generation rate than the hollow single crystals suggests the dominant role of a higher conduction band edge in determining CH<sub>4</sub> generation. The work by Inoue et al. also demonstrated a similar trend by estimating the photo-reduction of CO<sub>2</sub> on semiconductors with different conduction band edges.<sup>25</sup> On the other hand, it was proposed that the transfer of photoexcited charge carriers between different facets may occur because of different electronic band structure of facets.<sup>26–28</sup> In our case, such carrier transfer between major {101} and minor high-index facet of the hollow single crystals and mesocrystals may also contribute to the separation of charge carriers and thus photocatalytic activity, to some extent.

## CONCLUSIONS

Hollow anatase TiO<sub>2</sub> single crystals and mesocrystals were synthesized via a new synthesis route featuring F<sup>-</sup>/PO<sub>4</sub><sup>3-</sup> as morphology controlling agent. As a result of the shortened bulk diffusion length of charge carriers and increased surface area, these hollow crystals show a much superior photocatalytic activity in O<sub>2</sub>/H<sub>2</sub> evolution from water splitting, CH<sub>4</sub> generation from photoreduction of CO<sub>2</sub> to solid single crystals. Furthermore, the hollow single crystals and mesocrystals show different photocatalytic reaction preference toward hydrogen or oxygen evolution from water splitting in the presence of an electron donor or acceptor.

## ASSOCIATED CONTENT

### Supporting Information

Further details are given in Figures S1, S2, and S3. This material is available free of charge via the Internet at <http://pubs.acs.org>.

## AUTHOR INFORMATION

### Corresponding Author

\*E-mail: [gangliu@imr.ac.cn](mailto:gangliu@imr.ac.cn).

### Funding

The authors thank the Major Basic Research Program, Ministry of Science and Technology of China (No. 2009CB220001), NSFC (Nos. 50921004, 51002160, 21090343, 51172243), Solar Energy Initiative of CAS for financial support. G.L. thanks the IMR SYNL-T.S. Kê Research Fellowship.

### Notes

The authors declare no competing financial interest.

## ACKNOWLEDGMENTS

The authors thank L. L. Zhang for her help in TEM characterization.

## REFERENCES

- (1) Liu, G.; Yu, J. C.; Lu, G. Q.; Cheng, H. M. *Chem. Commun.* **2011**, 47, 6763.
- (2) Fang, W. Q.; Gong, X. Q.; Yang, H. G. *J. Phys. Chem. Lett.* **2011**, 2, 725.
- (3) Yang, H. G.; Sun, C. H.; Qiao, S. Z.; Zou, J.; Liu, G.; Smith, S. C.; Cheng, H. M.; Lu, G. Q. *Nature* **2008**, 453, 638.
- (4) Han, X. G.; Kuang, Q.; Jin, M. S.; Xie, Z. X.; Zheng, L. S. *J. Am. Chem. Soc.* **2009**, 131, 3152.
- (5) Yang, H. G.; Liu, G.; Qiao, S. Z.; Sun, C. H.; Jin, Y. G.; Smith, S. C.; Zou, J.; Cheng, H. M.; Lu, G. Q. *J. Am. Chem. Soc.* **2009**, 131, 4078.
- (6) Zhang, D. Q.; Li, G. S.; Yang, X. F.; Yu, J. C. *Chem. Commun.* **2009**, 4381.
- (7) Liu, S. W.; Yu, J. G.; Jaroniec, M. *J. Am. Chem. Soc.* **2010**, 132, 11914.
- (8) Zheng, Z. K.; Huang, B. B.; Lu, J. B.; Qin, X. Y.; Zhang, X. Y.; Dai, Y. *Chem.—Eur. J.* **2011**, 17, 15032.
- (9) Wang, Z. Y.; Huang, B. B.; Dai, Y.; Liu, Y. Y.; Zhang, X. Y.; Qin, X. Y.; Wang, J. P.; Zheng, Z. K.; Cheng, H. F. *CrystEngComm* **2012**, 14, 1687.
- (10) Liu, G.; Pan, J.; Yin, L. C.; Irvine, J. T. S.; Li, F.; Tan, J.; Wormald, P.; Cheng, H. M. *Adv. Funct. Mater.* **2012**, DOI: 10.1002/adfm.201200414.
- (11) Pan, J.; Liu, G.; Lu, G. Q.; Cheng, H. M. *Angew. Chem., Int. Ed.* **2011**, 50, 2133.
- (12) Tachikawa, T.; Wang, N.; Yamashita, S.; Cui, S. C.; Majima, T. *Angew. Chem., Int. Ed.* **2010**, 49, 8593.
- (13) Pan, J. H.; Han, G.; Zhou, R.; Zhao, X. S. *Chem. Commun.* **2011**, 47, 6942.
- (14) Pan, J.; Wu, X.; Wang, L. Z.; Liu, G.; Lu, G. Q.; Cheng, H. M. *Chem. Commun.* **2011**, 47, 8361.
- (15) Tartaj, P. *Chem. Commun.* **2011**, 47, 256.
- (16) Tartaj, P.; Amarilla, J. M. *Adv. Mater.* **2011**, DOI: 10.1002/adma.201103168.
- (17) Diebold, U. *Surf. Sci. Rep.* **2003**, 48, 53.
- (18) Jiang, H. B.; Cuan, Q. A.; Wen, C. Z.; Xing, J.; Wu, D.; Gong, X. Q.; Li, C. Z.; Yang, H. G. *Angew. Chem., Int. Ed.* **2011**, 50, 3764.
- (19) Yu, J. C.; Yu, J. G.; Ho, W. K.; Jiang, Z. T.; Zhang, L. Z. *Chem. Mater.* **2002**, 14, 3808.
- (20) Liu, G.; Sun, C. H.; Yang, H. G.; Smith, S. C.; Wang, L. Z.; Lu, G. Q.; Cheng, H. M. *Chem. Commun.* **2010**, 46, 755.
- (21) Wang, Y.; Zhang, H. M.; Han, Y. H.; Liu, P. R.; Yao, X. D.; Zhao, H. J. *Chem. Commun.* **2011**, 47, 2829.
- (22) Chen, G. Z.; Zhu, F. F.; Sun, X. A.; Sun, S. X.; Chen, R. P. *CrystEngComm* **2011**, 13, 2904.
- (23) Yu, J. C.; Zhang, L. Z.; Zheng, Z.; Zhao, J. C. *Chem. Mater.* **2003**, 15, 2280.
- (24) Xie, Y. P.; Liu, G.; Cheng, H. M. *J. Mater. Chem.* **2012**, 22, 6746.
- (25) Inoue, T.; Fujishima, A.; Konishi, S.; Honda, K. *Nature* **1979**, 277, 637.

- (26) Ohno, T.; Sarukawa, K.; Matsumura, M. *New J. Chem.* **2002**, *26*, 1167.
- (27) Zheng, Z. K.; Huang, B. B.; Wang, Z. Y.; Guo, M.; Qin, X. Y.; Zhang, X. Y.; Wang, P.; Dai, Y. *J. Phys. Chem. C* **2009**, *113*, 14448.
- (28) D'Arienzo, M.; Carbajo, J.; Bahamonde, A.; Crippa, M.; Polizzi, S.; Scotti, R.; Wahba, L.; Morazzoni, F. *J. Am. Chem. Soc.* **2011**, *133*, 17652.